IEEE Access
Multidisciplinary ⋮ Rapid Review ⋮ Open Access Journal

Received October 20, 2021, accepted November 3, 2021, date of publication November 11, 2021,
date of current version November 19, 2021.

Digital Object Identifier 10.1109/ACCESS.2021.3127695

A Fast Barzilai-Borwein Gradient Projection for Sparse Reconstruction Algorithm Based on 3D Modeling: Application to ERT Imaging

SHOUXIAO LI[1], HUAXIANG WANG[2], (Senior Member, IEEE), TONGHAI LIU[1], ZIQIANG CUI[2], (Member, IEEE), JOANNA N. CHEN[3], AND ZIHAN XIA[2]

[1]College of Computer and Information Engineering, Tianjin Agricultural University, Tianjin 300392, China
[2]School of Electrical and Information Engineering, Tianjin University, Tianjin 300072, China
[3]College of Science, Tianjin University of Technology, Tianjin 300384, China

Corresponding author: Shouxiao Li (lsxtjau@163.com)

This work was supported in part by the National Natural Science Foundation of China under Grant 11701420, Grant 61671319, and Grant 61627803; in part by the Natural Science Foundation Project of Tianjin Municipal Education Committee under Grant 2018KJ193 and Grant 2017KJ243; and in part by the Science and Technology Support Key Projects of Tianjin under Grant 20YFZCSN00220.

ABSTRACT Image reconstruction for electrical resistance tomography (ERT) is an ill-posed inverse problem. L_1 regularization is used to solve the inverse problem. An effective method of Barzilai-Borwein gradient projection for sparse reconstruction (GPSR-BB) can resolve the inverse problem into bound-constrained quadratic programming and achieve a gradient projection with line search. However, it is computationally expensive to solve the problem when the data dimension is substantial. Hence, a projection method is employed and combined with the GPSR-BB algorithm to improve the real-time performance. The problem can be mainly solved in the Krylov subspace. For comparison, another L_1 regularization GPSR-BB method based on the truncated singular value decomposition is also conducted. Both simulation (with 3D modeling) and experimental results demonstrate the new method's effectiveness in reducing the computational time and improving the image quality.

INDEX TERMS Electrical resistance tomography, projection method, L_1 regularization method, gradient projection for sparse reconstruction.

I. INTRODUCTION

Electrical resistance tomography (ERT), which reflects the changes of electrical conductivity distribution in the control volume based on the measured voltage [1]–[3], is considered a novel sensing technique. Due to the advantages of non-radiation, non-invasive and fast response, it has been successfully applied in several fields, such as industrial process imaging [4]–[6], medical imaging [7], [8], and geophysical surveying [9].

The inverse problem for ERT is ill-posed and ill-conditioned due to the property of the sensitivity matrix. Regularization has been widely used to overcome ill-posedness in ERT, which can be divided into two main types: projection methods [10], [11] and penalty methods. Projection methods include the truncated singular value decomposition (TSVD), the Ivanov regularization, and so on.

The associate editor coordinating the review of this manuscript and approving it for publication was Ge Wang.

The penalty methods [12]–[15] include Tikhonov regularization, L_1 regularization, and so on. Tikhonov regularization is commonly used among these methods. However, it is plagued by the smoothness effect being an L_2-norm regularization. The sparse reconstruction method with L_1-norm, having wide application in compressed sensing [16]–[18], was used to solve the electrical tomography (ET) inverse problem. Tehrani *et al.* proposed a new L_1 regularization method combining the basis pursuit denoising and the least absolute shrinkage and selection operator (LASSO) for electrical impedance tomography [19]. Ye *et al.* presented a new sparsity regularization algorithm for electrical capacitance tomography (ECT) using an unconventional basis to improve the image quality [20]. Fan *et al.* proposed an improved method based on the separable approximation method by using adaptive step size to improve the calculation speed of sparse regularization [21]. Zhang *et al.* [22] presented a modified orthogonal matching pursuit method for the ERT inverse problem. Shi *et al.* [23] developed

a Landweber-based non-convex L_1 regularization method for the ERT image reconstruction to get high quality images. Zhang *et al.* applied Barzilai-Borwein gradient projection for sparse reconstruction (GPSR-BB) to ECT image reconstruction [24]. The experimental results show that the quality of the images can be enhanced obviously. However, the L_1 method is a substantially time-consuming method due to the need to solve large-dimensional matrix equations repeatedly.

An effective way to reduce the computational cost for the image reconstruction is the projection method, i.e., the TSVD method. The idea of the method is to project the solution into a lower dimension subspace by omitting the unimportant part in the subspace. The projection method can be combined with other methods to improve the quality of reconstructed images. The projected conjugate gradient method is presented and applied to the image reconstruction of ECT, which improves both image quality and real-time performance [25]. Zhao *et al.* proposed a hybrid reconstruction algorithm for ERT by combining two regularization algorithms to improve the imaging quality and reduce the computational time [26]. In this paper, a novel method based on GPSR-BB is proposed for ERT, which is combined with the GPSR-BB and the projection method. The proposed method consists of two parts: part 1 is the projection transformation, part 2 is the sparse reconstruction, which is solved by the GPSR-BB in the Krylov subspace. To the best of our knowledge, it is the first time that this new sparse regularization method has been applied to ERT image reconstruction. Both numerical simulations and experiments on liquid/solid two-phase flow measurement are conducted to verify the new method's effectiveness.

This paper is organized as follows. In section II, we introduce the principle of ERT. We present GPSR-BB for ERT, GPSR-BB based on the TSVD method, and GPSR-BB based on Krylov subspace in section III. In section IV, we discuss the simulations and experiments of the proposed method. Finally, the conclusions are provided in section V.

II. PRINCIPLE OF ERT

An ERT system consists of sensing electrodes, a data acquisition system, and an image reconstruction and visualization unit, as shown in Fig. 1.

The mathematical model of ERT can be represented by

$$\nabla \cdot (\sigma \cdot \nabla \phi) = 0, \tag{1}$$

where ∇ is the gradient operator, σ is the conductivity distribution, and ϕ stands for potential distribution in the control volume. The relationship between σ and measured voltage φ on boundary sensors can be described as

$$\varphi = f(\sigma; D), \tag{2}$$

where D is the injected current density. If there is a slight change of conductivity, equation (2) can be written as

$$\Delta\varphi = \left.\frac{df(\sigma; D)}{d\sigma}\right|_{\sigma=\sigma_0} \Delta\sigma. \tag{3}$$

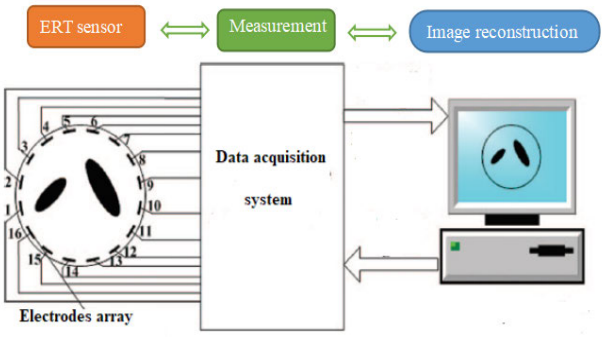

FIGURE 1. Configuration of ERT system.

For the convenience of calculation, equation (3) can be described as follows:

$$\mathbf{y} = \mathbf{S}\mathbf{x}, \tag{4}$$

where $\mathbf{S} \in \mathbf{R}^{m\times n}$ is the Jacobian matrix, $\mathbf{x} \in \mathbf{R}^{n\times 1}$ is the change in conductivity, and $\mathbf{y} \in \mathbf{R}^{m\times 1}$ is the changes of measured voltages. In ERT, $\mathbf{S}$ is usually calculated by a sensitivity method.

The inverse problem of ERT is ill-posed. Tikhonov regularization replaces the inverse problem of (4) with a minimization one. It leads to the expression

$$\hat{\mathbf{x}} = \arg\min_{\mathbf{x}} \|\mathbf{S}\mathbf{x} - \mathbf{y}\|_2^2 + \lambda\|\mathbf{x}\|_2^2, \tag{5}$$

where λ is the regularization coefficient, $\|.\|_2$ stands for the L_2-norm. To overcome the excessive smoothness of the L_2-norm method, the L_1 regularization method is set up as

$$\hat{\mathbf{x}} = \arg\min_{\mathbf{x}} \frac{1}{2}\|\mathbf{S}\mathbf{x} - \mathbf{y}\|_2^2 + \lambda\|\mathbf{x}\|_1, \tag{6}$$

where $\|.\|_1$ stands for the L_1-norm, i.e., $\|\mathbf{x}\|_1 = \sum_i^n |x_i|$ and λ is the regularization coefficient. This optimization form is widely used in compressed sensing theory and sparse approximation theory. The modified GPSR-BB, comparatively an effective method for dealing with this problem (6), is adopted in this paper.

III. METHODS

A. NORMALIZATION

In order to improve the image quality and reduce systematic errors in the measurement system, the sensitivity needs to be normalized. The sensitivity for each electrode pair is normalized by summing sensitivity's all elements as follows:

$$S_{N,ij} = \frac{S_{i,j}}{\sum_{i=1}^{m} S_{i,j}}. \tag{7}$$

B. GPSR-BB FOR ERT

The approach is to express (6) as a quadratic program which is worked by splitting image gray matrix $\mathbf{x}$ into positive and negative parts. We introduce vectors $\mathbf{p}$ and $\mathbf{q}$ and make the substitution of $\mathbf{x}$, enforcing a nonnegativity

constraint on each part [27].

$$\begin{cases} \mathbf{x} = \mathbf{p} - \mathbf{q}, \mathbf{p} \geq 0, \mathbf{q} \geq 0 \\ \|\mathbf{x}\|_1 = \mathbf{1}_n^T \mathbf{p} + \mathbf{1}_n^T \mathbf{q}, \end{cases} \tag{8}$$

where $\mathbf{1}_n = [1, 1, 1 \cdots, 1]^T$. And the quadratic program of equation (6) can be described as follows:

$$\min_{\mathbf{p},\mathbf{q}} \frac{1}{2}\|\mathbf{y} - \mathbf{S}(\mathbf{p} - \mathbf{q})\|_2^2 + \lambda \mathbf{1}_n^T \mathbf{p} + \lambda \mathbf{1}_n^T \mathbf{q},$$
$$s.t.\ \mathbf{p} \geq 0, \mathbf{q} \geq 0. \tag{9}$$

From [27], the equation (9) can be written in the standard bound-constrained quadratic program (BCQP)

$$\min_{\mathbf{z}} \mathbf{c}^T \mathbf{z} + \frac{1}{2}\mathbf{z}^T \mathbf{B}\mathbf{z} \equiv F(\mathbf{z}), s.t. \mathbf{z} \geq 0, \tag{10}$$

where

$$\mathbf{z} = \begin{bmatrix} \mathbf{p} \\ \mathbf{q} \end{bmatrix}, \ \mathbf{b} = \mathbf{S}^T \mathbf{y}, \ \mathbf{c} = \lambda \mathbf{1}_{2n} + \begin{bmatrix} \mathbf{b} \\ -\mathbf{b} \end{bmatrix}$$

and

$$\mathbf{B} = \begin{bmatrix} \mathbf{S}^T\mathbf{S} & -\mathbf{S}^T\mathbf{S} \\ -\mathbf{S}^T\mathbf{S} & \mathbf{S}^T\mathbf{S} \end{bmatrix}.$$

To solve equation (10), we first choose a scalar parameter $\alpha^{(t)} > 0$ and let

$$\boldsymbol{\theta}^{(t)} = (\mathbf{z}^{(t)} - \alpha^{(t)} \nabla F(\mathbf{z}^{(t)}))_+. \tag{11}$$

After that, we choose a second scalar parameter $\eta^{(t)} \in [0, 1]$ and let

$$\mathbf{z}^{(t+1)} = \mathbf{z}^{(t)} + \eta^{(t)}(\boldsymbol{\theta}^{(t)} - \mathbf{z}^{(t)}). \tag{12}$$

In the GPSR-BB algorithm, it calculates each step by $\boldsymbol{\delta}^{(t)} = -\mathbf{H}_t^{-1} \nabla F(\mathbf{z}^{(t)})$, where $\mathbf{H}_t$ is the approximation to the Hessian of F at $\mathbf{z}^{(t)}$. In the Barzilai-Borwein method, a simple choice for the approximation $\mathbf{H}_t$ is to set $\mathbf{H}_t = \xi^{(t)}\mathbf{I}$, where $\xi^{(t)}$ is chosen so that the approximation $\mathbf{H}_t$ has the similar behavior to the true Hessian, that is

$$\nabla F(\mathbf{z}^{(t)}) - \nabla F(\mathbf{z}^{(t-1)}) \approx \xi^{(t)}[\mathbf{z}^{(t)} - \mathbf{z}^{(t-1)}]. \tag{13}$$

The update equation under the unconstrained condition can be shown:

$$z^{(t+1)} = \mathbf{z}^{(t)} - (\xi^{(t)})^{-1} \nabla F(\mathbf{z}^{(t)}). \tag{14}$$

$\alpha^{(t)} = (\xi^{(t)})^{-1}$ should be restricted to the interval $[\alpha_{min}, \alpha_{max}]$.

The GPSR-BB algorithm can be defined as follows:

Step 0 (initialization): Selecting parameters α_{min}, α_{max}, $\alpha^{(0)}$, setting $t = 0$ and $\mathbf{z}^{(0)}$;

Step 1: The step length calculation:

$$\boldsymbol{\delta}^{(t)} = (\mathbf{z}^{(t)} - \alpha^{(t)} \nabla F(\mathbf{z}^{(t)}))_+ - \mathbf{z}^{(t)}; \tag{15}$$

Step 2 (line search): On the condition of the scalar parameter $\eta^{(t)} \in [0, 1]$, finding the $\eta^{(t)}$ that can minimize $F(\mathbf{z}^{(t)} + \eta^{(t)}\boldsymbol{\delta}^{(t)})$, and setting $\mathbf{z}^{(t+1)} = \mathbf{z}^{(t)} + \eta^{(t)}\boldsymbol{\delta}^{(t)}$;

Step 3 (update scalar parameter α): Let

$$\gamma^{(t)} = (\boldsymbol{\delta}^{(t)})^T \mathbf{B} \boldsymbol{\delta}^{(t)}, \tag{16}$$

if $\gamma^{(t)} = 0$, we set $\alpha^{(t+1)} = \alpha_{max}$, otherwise

$$\alpha^{(t+1)} = \text{mid}\left\{\alpha_{min}, \frac{\|\boldsymbol{\delta}^{(t)}\|_2^2}{\gamma^{(t)}}, \alpha_{max}\right\};$$

Step 4: Perform convergence test and terminate when $|\frac{F(\mathbf{z})^{(t+1)} - F(\mathbf{z})^{(t)}}{F(\mathbf{z})^{(t)}}| \leq$ tolP, where tolP is a small parameter; otherwise, we set $t \leftarrow t + 1$, and then return to Step 1.

The values of $\alpha_{min} = 10^{-30}$ and $\alpha_{max} = 10^{30}$ are set as the default values as suggested in [27] to implement the GPSR-BB. In order to ensure convergence of the solution, the iterations are limited to 10^4. The choice of λ is important, which determines the image quality and computation speed. The selection of λ can be determined by the sparse degree of the problem which $\|\mathbf{S^T y}\|_\infty$ reflects. In this paper, we set $\lambda = 0.01\|\mathbf{S^T y}\|_\infty$.

C. GPSR-BB BASED ON TRUNCATED SINGULAR VALUE DECOMPOSITION METHOD (TGPSR-BB)

A solution to the problem can be found effectively through projection in a low-dimensional subspace. A TSVD method is a commonly used projection method, which directly modifies the problem into the rank deficient approximation [10]. An ERT solution is usually unstable, which is sensitive to the measured noise. Using the SVD of $\mathbf{S} = \mathbf{U}\Lambda\mathbf{V}^T$, we can obtain a truncated operator

$$\mathbf{S}_w = \mathbf{U}_w \Lambda_w \mathbf{V}_w^T,$$

where $\mathbf{U}_w = [\mathbf{u}_1, \cdots, \mathbf{u}_w]$, $\mathbf{V}_w = [\mathbf{v}_1, \cdots, \mathbf{v}_w]$, and $\Lambda_w = diag(\sigma_1, \sigma_2, \cdots, \sigma_w)$. The small singular values of $\mathbf{S}$ can be neglected for the noise involved.

The GPSR-BB based on the TSVD method (TGPSR-BB) is as follows:

Step 0 (Normalization): $S_{N,ij} = \frac{S_{i,j}}{\sum_{i=1}^{m} S_{i,j}}$, let $\mathbf{S}_N \rightarrow \mathbf{S}$;

Step 1: Computing $\mathbf{S} = \mathbf{U}\Lambda\mathbf{V}^T$, $\mathbf{S}$ is $m \times n$ matrix. Selecting the maximum w singular values and calculating $\Lambda_w = diag(\sigma_1, \sigma_2, \cdots, \sigma_w)$, $\sigma_1 \geq \sigma_2 \geq \cdots \geq \sigma_w$;

Step 2: The realization of the new sensitivity matrix

$$\mathbf{S}_{new} = \mathbf{U}\begin{bmatrix} \Lambda_w & 0 \\ 0 & 0 \end{bmatrix}\mathbf{V}^T$$

and then the adoption of new objective function $\min_{\mathbf{x}} F(\mathbf{x}) = \frac{1}{2}\|\mathbf{S}_{\text{new}}\mathbf{x} - \mathbf{y}\|_2^2 + \lambda\|\mathbf{x}\|_1$;

Step 3: Getting the solution based on the GPSR-BB algorithm.

The selection of w is important to the solution of the TGPSR-BB algorithm. The singular values for the Jacobian matrix $\mathbf{S}$ are shown in Fig. 2. In this paper, we set $w = 50$.

D. GPSR-BB BASED ON KRYLOV SUBSPACE (KGPSR-BB)

A novel GPSR-BB method based on Krylov subspace is presented for the real-time performance improvement of ERT. To reduce computational time, the KGPSR-BB can project $\mathbf{S}$ and $\mathbf{y}$ into the Krylov subspace. The Krylov subspace of

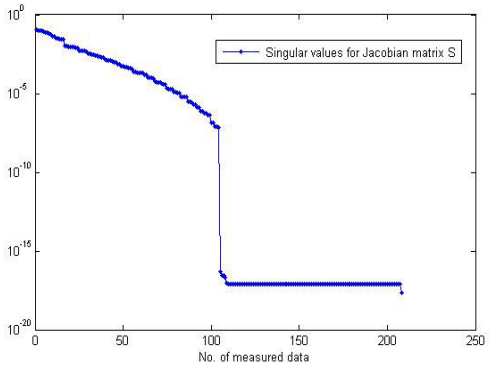

FIGURE 2. Singular values for S.

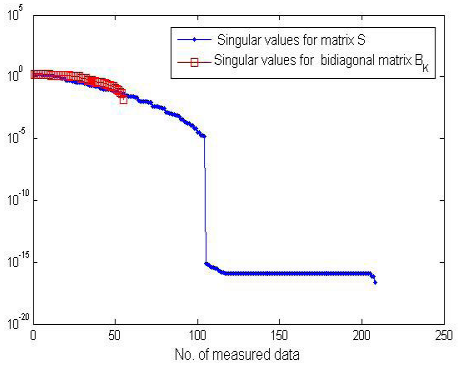

FIGURE 3. Singular values for S and $\mathbf{B}_k$ on a logarithmic scale.

dimension k is set up as [10]

$$K_k\left(\mathbf{S}^{\mathrm{T}}\mathbf{S}, \mathbf{S}^{\mathrm{T}}\mathbf{y}\right) \equiv \mathrm{span}\left\{\mathbf{S}^{\mathrm{T}}\mathbf{y}, \left(\mathbf{S}^{\mathrm{T}}\mathbf{S}\right)\mathbf{S}^{\mathrm{T}}\mathbf{y}, \left(\mathbf{S}^{\mathrm{T}}\mathbf{S}\right)^2\mathbf{S}^{\mathrm{T}}\mathbf{y}, \cdots, \left(\mathbf{S}^{\mathrm{T}}\mathbf{S}\right)^{k-1}\mathbf{S}^{\mathrm{T}}\mathbf{y}\right\}. \quad (17)$$

To get the orthonormal subspace $\mathbf{W}_k$, a Lanczos bidiagonalization method is utilized to complete the orthonormal decomposition of K_k [28]. The method creates a lower bidiagonal matrix and two orthogonal matrices. The relationship is

$$\mathbf{S}\mathbf{V}_k = \mathbf{U}_{k+1}\mathbf{B}_k, \quad (18)$$

where $\mathbf{U}_{k+1} \in \mathbf{R}^{m\times(k+1)}$ stands for an orthogonal basis of $K_{k+1}\left(\mathbf{S}\mathbf{S}^{\mathrm{T}}, \mathbf{y}\right)$, $\mathbf{B}_k \in \mathbf{R}^{(k+1)\times k}$ stands for a lower bidiagonal matrix, and the matrix $\mathbf{V}_k \in \mathbf{R}^{n\times k}$ is an orthogonal basis of $K_k\left(\mathbf{S}^{\mathrm{T}}\mathbf{S}, \mathbf{S}^{\mathrm{T}}\mathbf{y}\right)$. Then the objective function can be transformed to

$$\mathbf{g} = \arg\min_{\mathbf{g}}\left\{\|\mathbf{S}\mathbf{W}_k\mathbf{g} - \mathbf{y}\|_2^2 + \lambda\|\mathbf{W}_k\mathbf{g}\|_1\right\}, \quad (19)$$

$$\mathbf{x} = \mathbf{W}_k\mathbf{g}. \quad (20)$$

We set $\mathbf{W}_k = \mathbf{V}_k$, the equation (19) can be written as

$$\begin{aligned}&\|\mathbf{S}\mathbf{V}_k\mathbf{g} - \mathbf{y}\|_2^2 + \lambda\|V_k\mathbf{g}\|_1\\ &= \|\mathbf{U}_{k+1}\mathbf{B}_k\mathbf{g} - \mathbf{y}\|_2^2 + \lambda\|\mathbf{V}_k\mathbf{g}\|_1\\ &= \left\|\mathbf{U}_{k+1}^{\mathrm{T}}\left(\mathbf{U}_{k+1}\mathbf{B}_k\mathbf{g} - \mathbf{y}\right)\right\|_2^2 + \lambda\|\mathbf{V}_k\mathbf{g}\|_1\\ &= \left\|\mathbf{B}_k\mathbf{g} - \mathbf{U}_{k+1}^{\mathrm{T}}\mathbf{y}\right\|_2^2 + \lambda\|\mathbf{V}_k\mathbf{g}\|_1. \end{aligned} \quad (21)$$

The alternative form of the equation (19) is

$$\mathbf{g} = \arg\min_{\mathbf{g}}\left\{\left\|\mathbf{B}_k\mathbf{g} - \mathbf{U}_{k+1}^{\mathrm{T}}\mathbf{y}\right\|_2^2 + \lambda\|\mathbf{V}_k\mathbf{g}\|_1\right\}. \quad (22)$$

In equation (22), $\mathbf{V}_k$ and $\mathbf{U}_{k+1}$ can be calculated by the Lanczos bidiagonalization method. The GPSR-BB based on Krylov subspace (KGPSR-BB) solves the inverse problem of ERT by four steps:

Step 0 (Normalization): $S_{N,ij} = \frac{S_{i,j}}{\sum_{i=1}^{m} S_{i,j}}$, let $\mathbf{S}_N \to \mathbf{S}$;

Step 1: Projecting $\mathbf{S}$ and $\mathbf{y}$ to low dimensional subspaces;

Step 2: Solving $\mathbf{g}$ by the GPSR-BB method;

Step 3: The inverse projection transformation of the solution in Step 2 to obtain the real solution $\mathbf{x} = \mathbf{V}_k\mathbf{g}$.

It is worth noting that the first two steps can be done before iteration to cut the computational time. The singular values of $\mathbf{S}$ decay quickly to zero owing to the ill-posedness. According to Fig. 3, we can see that the first 55 singular values of the bidiagonal matrix $\mathbf{B}_k$ and the matrix $\mathbf{S}$ are almost the same. Therefore, we set $k = 55$.

IV. RESULTS

The proposed method was proved effective by simulation and experimental results. A brief introduction on TIK, TGPSR-BB, KGPSR-BB for the Tikhonov regularization, GPSR-BB based on TSVD method, and GPSR-BB based on Krylov subspace method is included.

A. NUMERICAL SIMULATION

The simulations were carried out in a COMSOL Multiphysics and Matlab environment on a PC equipped with an Intel Core i7 CPU of 2.7 GHz. The result of the forward problem calculation in the 3D model is more accurate than that in a 2D model. Thus, a 3D ERT sensor model is constructed in COMSOL to solve the forward problem. As shown in Fig. 4, the radius of the model is 10 cm, and the height is 10 cm. 16 circular electrodes with a radius of 1cm are located around the cylinder at the central height. A mesh with tetrahedron of the homogeneous field is generated for the forward problem, as shown in Fig. 4(a). Fig. 4(b) shows that the mesh with 812 square elements is used for the inverse problem. The five 3D models of the ERT sensor are established in Fig. 5. The tetrahedral mesh number can be obtained in the forward problem, which is 67473, 68747, 70120, 67520, and 64419 in models (I), (II), (III), (IV), and (V), respectively. The measured voltages on boundary sensors are simulated by the complete electrode model made to have adjacent stimulation and measurement patterns. In the simulation, the conductivity of the background and the objects are set as 1 S/m and 3 S/m, respectively.

The Landweber, TIK, TwIST [29], GPSR-BB, TGPSR-BB, and KGPSR-BB were used to image the middle part of the ERT sensor, as shown in Fig. 6. Selections of λ

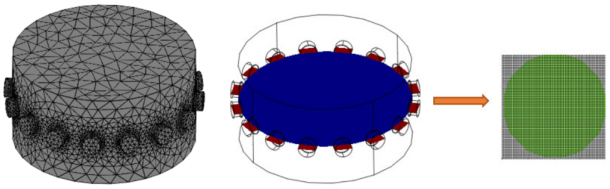

(a) (b)

FIGURE 4. Meshes. (a) Mesh for the forward problem of ERT. (b) Mesh for the inverse problem of ERT.

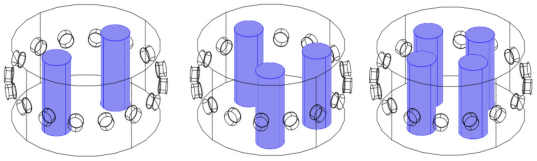

(a) model(I) (b) model(II) (c) model(III)

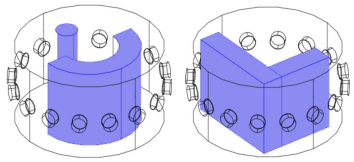

(d) model(IV) (e) model(V)

FIGURE 5. 3D modeling of ERT sensor.

TABLE 1. Values of λ for different methods.

Method	The value of λ
TIK	0.01
TwIST	10^{-9}
GPSR − BB	$0.01\|\mathbf{S^T y}\|_\infty$
TGPSR − BB	$0.01\|\mathbf{S^T y}\|_\infty$
KGPSR − BB	$\|\mathbf{S^T y}\|_\infty$

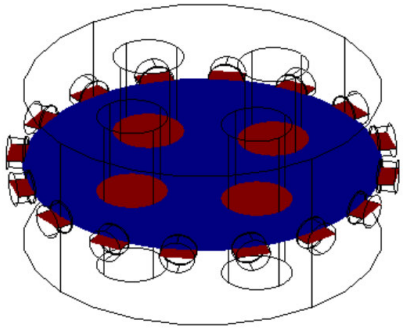

FIGURE 6. Section of 3D modeling.

for different methods are listed in Table 1. The number of iterations for the Landweber and the TIK is selected as 100 unanimously.

The criteria adopted for a quantitative evaluation of the result are the correlation coefficient (CC) and the mean square error (MSE) between the image and the model. The definition of CC and MSE can be seen in (23) and (24), respectively [20]. The higher the CC and the lower the MSE

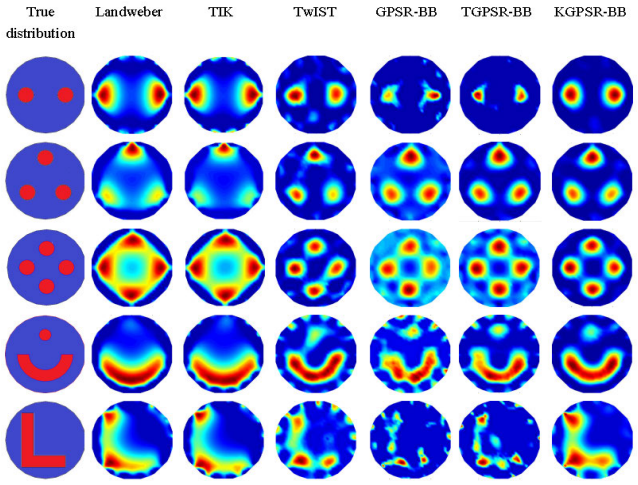

FIGURE 7. Image reconstructions of simulated data with 1% noise, in conductivity contrast of 1:3.

mean, the more favorable results of image reconstruction.

$$\mathrm{CC} = \frac{\sum_{i=1}^{N} (\mathbf{x}_i - \overline{\mathbf{x}}) \left(\mathbf{x}_i{}^* - \overline{\mathbf{x}}^*\right)}{\sqrt{\sum_{i=1}^{N} (\mathbf{x}_i - \overline{\mathbf{x}})^2 \sum_{i=1}^{N} \left(\mathbf{x}_i{}^* - \overline{\mathbf{x}}^*\right)^2}}, \tag{23}$$

$$\mathrm{MSE} = \frac{\|\mathbf{x} - \mathbf{x}^*\|_2^2}{N}, \tag{24}$$

where $\mathbf{x}^*$ is the real conductivity, $\mathbf{x}$ is the calculated one, $\overline{\mathbf{x}}$ and $\overline{\mathbf{x}^*}$ are the mean values of $\mathbf{x}$ and $\mathbf{x}^*$ respectively. N is the number of image pixels.

1) EFFECT OF NOISE INTENSITY

The reconstruction images are sensitive to measurement noise. This section tests the influences of different levels of noise on the six methods. Since the noise is inevitable in practical cases, the Gaussian random noise is added to the measured voltages in actual experiments as a noise simulation. The five conductivity distributions are shown in Fig. 7. The reconstruction results in Fig. 7 are conducted from the simulated data against 1% noise. The edge-preserving performance of KGPSR-BB is better than the other methods. 3% noise is added to the measured voltages to examine the noise robustness of the six methods. The reconstructions of the six methods are shown in Fig. 8. A few disturbances are seen in the reconstructed images compared with the images in Fig. 7. It can be seen from the results that the reconstructed image quality of TGPSR-BB is improved compared with GPSR-BB, and the KGPSR-BB presents the best quality of the reconstructed image. Fig. 8 shows that the results of reconstructed images based on KGPSR-BB are more stable, offering better quality in consideration of relatively high-level noise added to the measured voltages. Thus the KGPSR-BB is robust to noise.

For a quantitative evaluation of the reconstruction methods, the CC and MSE as defined in (23) and (24) are calculated corresponding to the images displayed in Fig. 9 and Fig. 10, respectively. Fig. 9 illustrates the CCs of the results

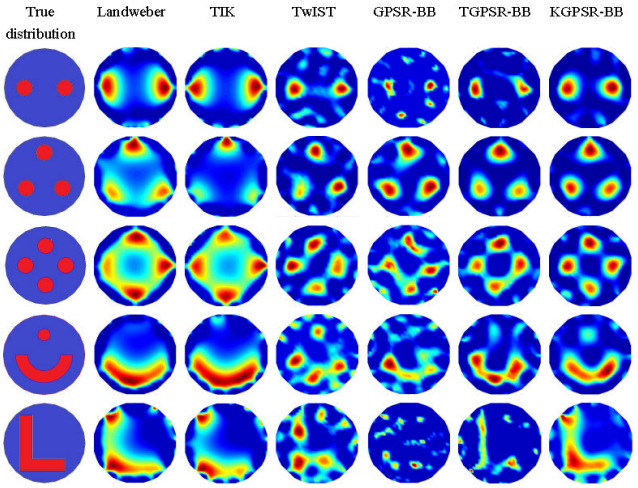

FIGURE 8. Image reconstructions of simulated data with 3% noise, in conductivity contrast of 1:3.

TABLE 2. The computational time of the methods for simulation with 1% noise.

Method	Computational time for each frame (s)				
	(I)	(II)	(III)	(IV)	(V)
Landweber	0.23	0.24	0.25	0.25	0.24
TIK	9.61	8.39	8.94	8.00	8.56
TwIST	0.043	0.042	0.069	0.11	0.15
GPSR-BB	0.59	0.043	0.12	0.13	2.34
TGPSR-BB	0.48	0.11	0.128	0.32	2.10
KGPSR-BB	0.074	0.031	0.102	0.098	0.044

in Figs. 7-8, which shows that the CC of a particular conductivity distribution decreases with the increase of noise level. Furthermore, the CC value obtained by KGPSR-BB changes minimally. With the increase of noise intensity, the CC value of KGPSR-BB is significantly higher than that of other methods. It can be seen that the added noise has no significant adverse effect on the image quality of the KGPSR-BB for all models. Fig. 10 shows the MSE value of KGPSR-BB is usually the smallest among the six methods with the noise of different levels. Consequently, the result of MSE is another evidence for the effectiveness and robustness of the KGPSR-BB. Comparison between Fig. 9 and Fig. 10 shows that the CC and MSE changes of the KGPSR-BB are the smallest. Hence, the method has the highest tolerance.

Table 2 and Table 3 show the computation time for different methods employed in Figs.7-8. It can be seen from Table 2 and Table 3 that the KGPSR-BB has a shorter imaging time than Landweber, TIK, and GPSR-BB methods, which means improved real-time performance.

2) EFFECT OF ELECTRICAL CONDUCTIVITY CONTRAST

As the conductivity of background and inclusions can also affect the image quality, different conductivity contrasts are required to test the proposed method. The parameters for the six methods are set the same as before. The conductivity of inclusions are set respectively to 10000 S/m for model (I), 1000 S/m for model (II), 100 S/m for model (III), 10 S/m

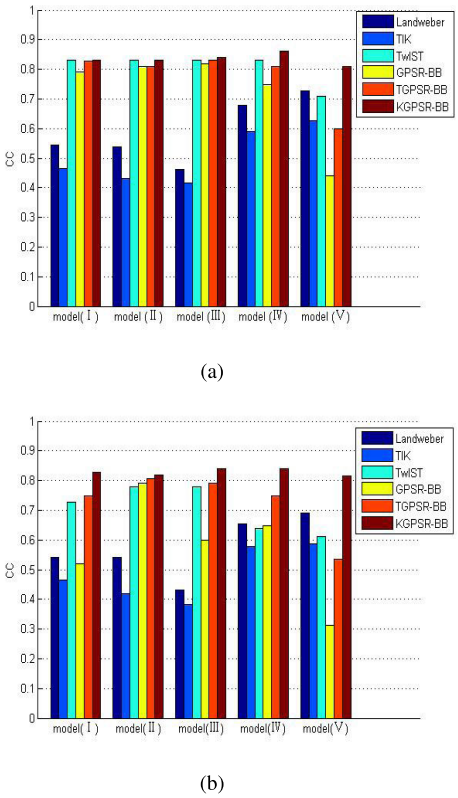

FIGURE 9. The CCs of the six methods for simulation with different noise levels, in conductivity contrast of 1:3. (a) with 1% noise (b) with 3% noise.

TABLE 3. The computational time of the methods for simulation with 3% noise.

Method	Computational time for each frame (s)				
	(I)	(II)	(III)	(IV)	(V)
Landweber	0.22	0.23	0.24	0.23	0.23
TIK	9.13	8.90	7.85	7.89	8.08
TwIST	0.080	0.032	0.035	0.050	0.167
GPSR-BB	1.65	0.029	0.20	0.14	1.65
TGPSR-BB	1.38	0.093	0.18	0.15	1.47
KGPSR-BB	0.060	0.028	0.089	0.067	0.052

for model (IV), and 0.1 S/m for model (V). The background conductivity is still 1 S/m for the five models.

The reconstructed images with 3% noise are plotted in Fig. 11. The six methods can reconstruct the surrounding conductivity distributions. It can be seen that the reconstructed images of the KGPSR-BB are with the slightest changes. Comparison between Fig. 8 and Fig. 11 indicates that the KGPSR-BB is more robust to the noise of 3% intensity than the other methods at these conductivity contrasts.

The quantitative results of the images are shown in Fig. 12. It can be seen in Fig. 12 (a) that the CC value of KGPSR-BB is usually the highest among the six methods considering conductivity contrasts. Fig. 12(b) shows that the MSE values of the proposed method are the smallest in the six algorithms presenting the best image quality consequently. A comparison among Fig. 9(b), Fig. 10(b), and Fig. 12 show that for most cases, the MSE and CC obtained by KGPSR-BB are nearly the same or within a slight range fluctuation.

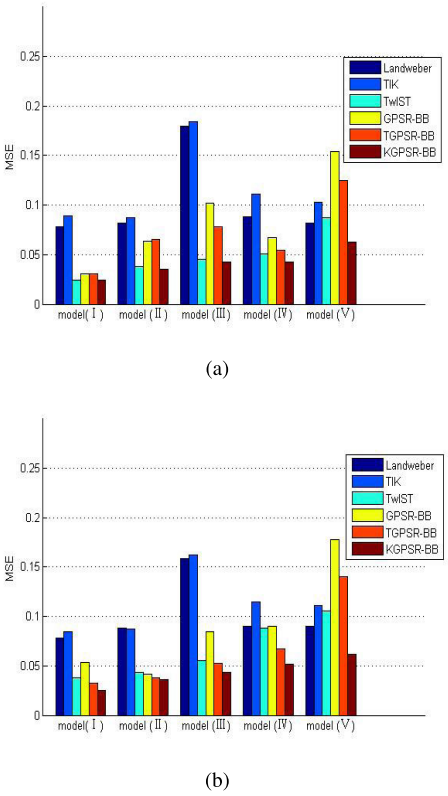

FIGURE 10. The MSEs of the six methods for simulation with different noise levels, in conductivity contrast of 1:3. (a) with 1% noise (b) with 3% noise.

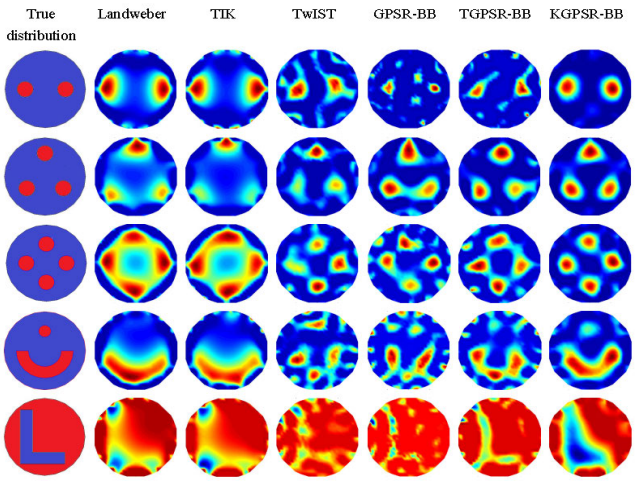

FIGURE 11. Image reconstructions with 3% noise when the conductivity ratios of background and inclusions are set as 1:10000, 1:1000, 1:100, 1:10, and 1:0.1.

The above analysis shows that the KGPSR-BB remains efficient against the background of different conductivity ratios.

3) EFFECT OF MESH SIZE

Another important factor, and one that influences the reconstruction images quality is the mesh size. The reconstructed

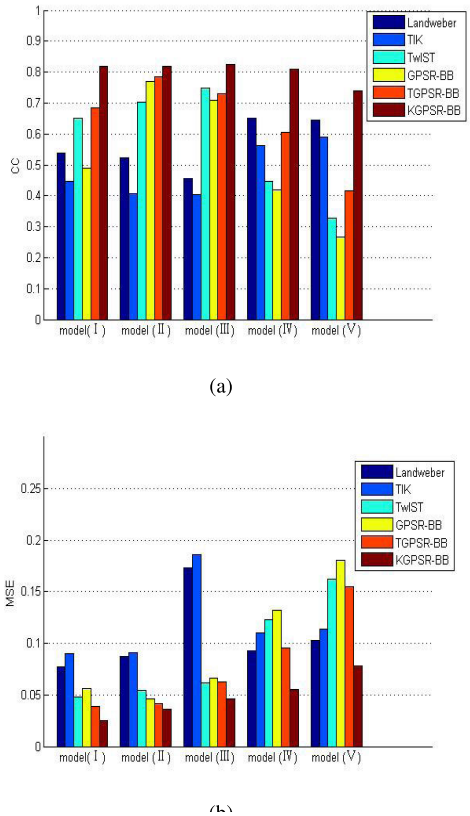

FIGURE 12. The CCs and MSEs of the six methods for different conductivity ratios with 3% noise. (a) CCs (b) MSEs.

mesh with 2472 square elements in a grid of 56×56 lines can be used to test the method's efficiency.

The simulated data from Fig. 8 are reconstructed in Fig. 13. It can be seen from Fig. 13 that the images of the KGPSR-BB have the best image quality. Comparison between Fig. 8 and Fig. 13 indicates that the KGPSR-BB is more robust than the other methods for different mesh sizes.

Table 4 and Table 5 show the CCs and MSEs corresponding to images in Fig. 8 and Fig. 13, respectively. They also indicate that the KGPSR-BB delivers better reconstruction results than the other methods.

As the reconstructed pixel number increases, more computation time is required. Table 6 shows the computation time for the methods in Fig. 13. It can be found in Table 6 that KGPSR-BB still gives the best real-time performance. Therefore, it is worth noting that the KGPSR-BB can strike a great balance between the computational time and the mesh size.

B. EXPERIMENTAL RESULTS

Static experiments on liquid/solid two-phase flow measurement were carried out to evaluate the performance of the KGPSR-BB. Fig. 14 shows the ERT system with the 16-electrode sensor designed by Tianjin University [30]. The excitation current in the ERT system is 2.5mA, 64 kHz sinusoidal AC. The size of the square electrode is 8×30 mm.

TABLE 4. CCs for 812 square elements in Fig.8 and 2472 square elements in Fig.13.

True distribution	Number of pixels	Landweber	TIK	TwIST	GPSR-BB	TGPSR-BB	KGPSR-BB
(I)	812	0.54	0.46	0.73	0.52	0.75	0.83
	2472	0.40	0.57	0.75	0.40	0.53	0.81
(II)	812	0.54	0.42	0.78	0.79	0.81	0.82
	2472	0.36	0.60	0.79	0.77	0.80	0.81
(III)	812	0.43	0.38	0.78	0.60	0.79	0.84
	2472	0.37	0.49	0.74	0.67	0.74	0.81
(IV)	812	0.65	0.58	0.64	0.65	0.75	0.84
	2472	0.51	0.70	0.78	0.52	0.71	0.82
(V)	812	0.69	0.59	0.61	0.31	0.53	0.81
	2472	0.56	0.77	0.64	0.21	0.29	0.80

TABLE 5. MSEs for 812 square elements in Fig.8 and 2472 square elements in Fig.13.

True distribution	Number of pixels	Landweber	TIK	TwIST	GPSR-BB	TGPSR-BB	KGPSR-BB
(I)	812	0.078	0.084	0.037	0.054	0.033	0.025
	2472	0.068	0.069	0.033	0.063	0.055	0.027
(II)	812	0.089	0.088	0.043	0.042	0.38	0.036
	2472	0.096	0.080	0.043	0.043	0.042	0.038
(III)	812	0.16	0.16	0.055	0.085	0.053	0.044
	2472	0.13	0.18	0.063	0.089	0.074	0.049
(IV)	812	0.090	0.11	0.088	0.090	0.068	0.052
	2472	0.12	0.080	0.062	0.12	0.084	0.054
(V)	812	0.090	0.11	0.11	0.18	0.14	0.062
	2472	0.12	0.078	0.11	0.21	0.21	0.068

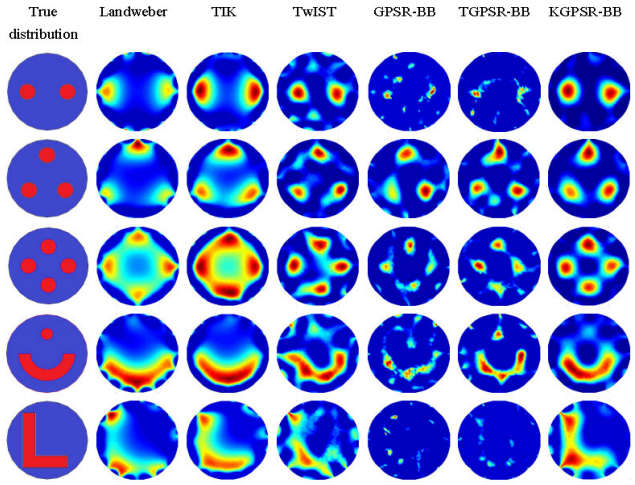

FIGURE 13. Image reconstructions with 3%noise by using a mesh with 2472 square elements.

TABLE 6. Computational time (s) of different methods in Fig. 13.

Method	Computational time for each frame (s)				
	(I)	(II)	(III)	(IV)	(V)
Landweber	0.77	0.77	0.75	0.68	0.63
TIK	277.6	247.2	241.9	243.6	225.1
TwIST	0.21	0.45	0.17	0.20	0.15
GPSR-BB	11.98	0.15	1.30	1.60	8.62
TGPSR-BB	8.09	0.22	1.42	1.71	6.36
KGPSR-BB	0.094	0.044	0.077	0.13	0.033

The parameters of the four experimental models are listed in Table 7. Materials in experiments, including perspex rods, the hollow tube, and Al_2O_3 particles, are placed in water (the conductivity of the water is 2.8×10^{-3} S/m). To facilitate

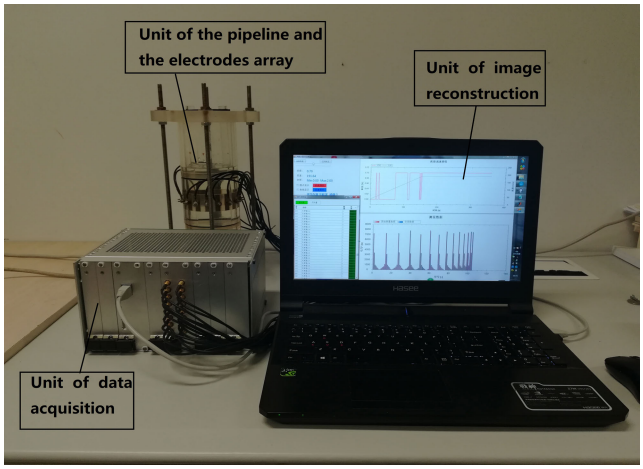

FIGURE 14. Experimental setup.

the positioning of perspex rods, we prepare a bracket via a 3D printer. The dimensions of the bracket are shown in Fig. 15. Six methods are used for image reconstruction. The values of λ for the TIK, TwIST, GPSR-BB, and KGPSR-BB methods are listed in Table 1. For TGPSR-BB, the regularization parameters are $\lambda = 0.01\|S^T y\|_\infty$ (model I, II, IV), $\lambda = 0.1\|S^T y\|_\infty$ (model III). The dimension of the Krylov subspace is set as 55.

The true distributions and reconstruction results from experimental data, using six methods, are shown in Fig. 16. The results show that the KGPSR-BB has superiority in preserving the edges of discontinuous parts in the reconstruction image. Compared to other methods, the reconstructed images of the KGPSR-BB have the best quality in both position and size.

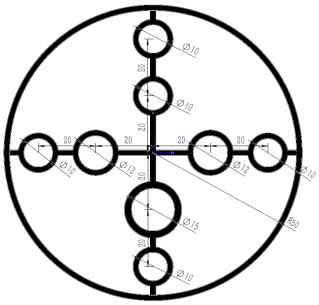

FIGURE 15. Dimensions of the bracket (mm).

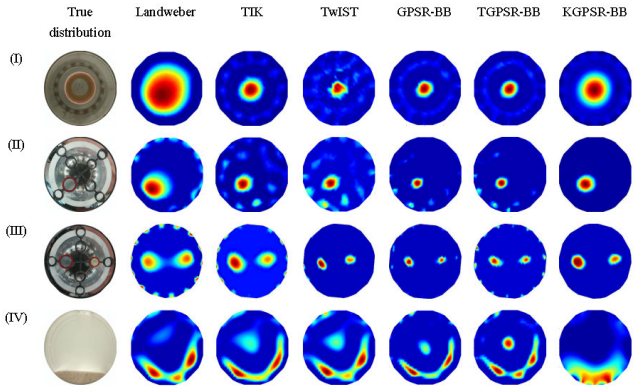

FIGURE 16. Reconstruction images from experimental data.

TABLE 7. Parameters of the practical models.

Model	Shape	Material	Size(mm)
(I)	Annular	PVC	Inner diameter=38 , Outer diameter= 40
(II)	Circle	Perspex	Diameter =15
(III)	Circle	Perspex	Diameter =15, Diameter =10
(IV)	Particles	Al_2O_3	Average particle size = 0.2

TABLE 8. Computational time (s) of different methods in Fig. 16.

Method	Computational time for each frame (s)			
	(I)	(II)	(III)	(IV)
Landweber	0.20	0.14	0.092	0.085
TIK	5.60	7.08	6.76	7.58
TwIST	0.086	0.22	1.22	0.056
GPSR-BB	0.20	0.19	0.052	0.22
TGPSR-BB	0.49	0.47	0.75	0.35
KGPSR-BB	0.095	0.022	0.027	0.027

The computational time is listed in Table 8. From the results, it can be seen that the KGPSR-BB can effectively reduce the computational time. Therefore, the KGPSR-BB can achieve effective reconstruction and improve real-time performance at the same time.

V. CONCLUSION

This paper presents an improved GPRS-BB method based on 3D modeling for ERT for fast and accurate ERT image reconstruction. Two regularization methods, the Krylov and GPSR-BB, are combined to improve the real-time performance of the method. A preconditioner based on normalization promotes the quality of reconstructed images. Another L_1 regularization method (TGPSR-BB) plays a role in comparison.

The KGPSR-BB method is found effective based on simulations and experiments. Five other methods are used to compare KGPSR-BB for different conductivity contrasts, noise intensities, and mesh sizes. By projecting **S** and **y** to a lower subspace, the KGPSR-BB reduces the computational time and presents better images because the CCs of KGPSR-BB are larger than the other methods. At the same time, the MSEs of KGPSR-BB are lower than the other methods. Four experimental models were adopted in the experiment, and the imaging results prove that KGPSR-BB can maintain a good balance between image quality and computational time.

In future work, the KGPSR-BB of this paper can be further extended to the improvement of other L_1-norm methods. This effective sparse regularization method would work for 3D image reconstruction in ECT and other kinds of tomography.

REFERENCES

[1] X. Zhang, W. Wang, G. Sze, D. Barber, and C. Chatwin, "An image reconstruction algorithm for 3-D electrical impedance mammography," *IEEE Trans. Med. Imag.*, vol. 33, no. 12, pp. 2223–2241, Dec. 2014.

[2] T. Rymarczyk, P. Tchorzewski, P. Adamkiewicz, K. Duda, J. Szumowski, and J. Sikora, "Practical implementation of electrical tomography in a distributed system to examine the condition of objects," *IEEE Sensors J.*, vol. 17, no. 24, pp. 8166–8186, Dec. 2017.

[3] J. Jia, H. Wang, and D. Millington, "Electrical resistance tomography sensor for highly conductive oil-water two-phase flow measurement," *IEEE Sensors J.*, vol. 17, no. 24, pp. 8224–8233, Dec. 2017.

[4] Z. Cao and L. Xu, "Direct image reconstruction for 3-D electrical resistance tomography by using the factorization method and electrodes on a single plane," *IEEE Trans. Instrum. Meas.*, vol. 62, no. 5, pp. 999–1007, May 2013.

[5] X. He, Y. Jiang, B. Wang, H. Ji, and Z. Huang, "An image reconstruction method of capacitively coupled electrical impedance tomography (CCEIT) based on DBSCAN and image fusion," *IEEE Trans. Instrum. Meas.*, vol. 70, pp. 1–11, 2021.

[6] Y. Tian, Z. Cao, D. Hu, X. Gao, L. Xu, and W. Yang, "A fuzzy PID-controlled iterative Calderon's method for binary distribution in electrical capacitance tomography," *IEEE Trans. Instrum. Meas.*, vol. 70, pp. 1–11, 2021.

[7] C. J. C. Trepte, C. R. Phillips, J. Solà, A. Adler, S. A. Haas, M. Rapin, S. H. Böhm, and D. A. Reuter, "Electrical impedance tomography (EIT) for quantification of pulmonary edema in acute lung injury," *Crit. Care*, vol. 20, no. 1, p. 18, Dec. 2015.

[8] F. S. Moura, J. C. C. Aya, A. T. Fleury, M. B. P. Amato, and R. G. Lima, "Dynamic imaging in electrical impedance tomography of the human chest with online transition matrix identification," *IEEE Trans. Biomed. Eng.*, vol. 57, no. 2, pp. 422–431, Feb. 2010.

[9] J. Doetsch, N. Linde, M. Pessognelli, A. G. Green, and T. Günther, "Constraining 3-D electrical resistance tomography with GPR reflection data for improved aquifer characterization," *J. Appl. Geophys.*, vol. 78, pp. 68–76, Mar. 2012.

[10] M. Jacobsen and P. C. Hansen, "Modular regularization algorithms," Ph.D. dissertation, Inform. Math. Model., Tech. Univ. Denmark, Denmark, 2004.

[11] Z. Cui, W. Qi, X. Qian, W. Fan, and W. Yang, "A review on image reconstruction algorithms for electrical capacitance/resistance tomography," *Sensor Rev.*, vol. 36, no. 4, pp. 429–445, 2016.

[12] J. P. Kaipio, V. Kolehmainen, M. Vauhkonen, and E. Somersalo, "Inverse problems with structural prior information," *Inverse Problems*, vol. 15, no. 3, p. 713, 1999.

[13] W. Q. Yang, "Image reconstruction algorithms for electrical capacitance tomography," *J. Tsinghua Univ.*, vol. 14, no. 4, pp. 478–484, 2004.

[14] Q. Wang, H. Wang, R. Zhang, J. Wang, Y. Zheng, Z. Cui, and C. Yang, "Image reconstruction based on L_1 regularization and projection methods for electrical impedance tomography," *Rev. Sci. Instrum.*, vol. 83, no. 10, Oct. 2012, Art. no. 104707.

[15] B. Y. Sun, S. H. Yue, Z. H. Hao, Z. Q. Cui, and H. X. Wang, "An improved Tikhonov regularization method for lung cancer monitoring using electrical impedance tomography," *IEEE Sensors J.*, vol. 19, no. 8, pp. 3049–3057, Apr. 2019.
[16] D. L. Donoho, "Compressed sensing," *IEEE Trans. Inf. Theory*, vol. 52, no. 4, pp. 1289–1306, Apr. 2006.
[17] E. J. Candès, "The restricted isometry property and its implications for compressed sensing," *Comp. Rendus Math.*, vol. 346, nos. 9–10, pp. 589–592, May 2008.
[18] J.-C. Ni, Q. Zhang, Y. Luo, and L. Sun, "Compressed sensing SAR imaging based on centralized sparse representation," *IEEE Sensors J.*, vol. 18, no. 12, pp. 4920–4932, Jun. 2018.
[19] J. N. Tehrani, A. McEwan, C. Jin, and A. van Schaik, "L1 regularization method in electrical impedance tomography by using the L1-curve (Pareto frontier curve)," *Appl. Math. Model.*, vol. 36, no. 3, pp. 1095–1105, Mar. 2012.
[20] J. Ye, H. Wang, and W. Yang, "Image reconstruction for electrical capacitance tomography based on sparse representation," *IEEE Trans. Instrum. Meas.*, vol. 64, no. 1, pp. 89–102, Jan. 2015.
[21] W. Fan, H. Wan, Q. Xue, Z. Cui, B. Sun, and Q. Wang, "Modified sparse regularization for electrical impedance tomography," *Rev. Sci. Instrum.*, vol. 87, no. 3, 2016, Art. no. 034702.
[22] W. Zhang, C. Tan, Y. Xu, and F. Dong, "Electrical resistance tomography image reconstruction based on modified OMP algorithm," *IEEE Sensors J.*, vol. 19, no. 14, pp. 5723–5731, Jul. 2019.
[23] Y. Shi, Q. Li, M. Wang, W. Liu, and Z. Tian, "A non-convex regularization method combined with Landweber method for image reconstruction in electrical resistance tomography," *Flow Meas. Instrum.*, vol. 79, Jun. 2021, Art. no. 101917.
[24] L. Zhang, Y. Zhai, and X. Wang, "Application of Barzilai–Borwein gradient projection for sparse reconstruction algorithm to image reconstruction of electrical capacitance tomography," *Flow Meas. Instrum.*, vol. 65, pp. 45–51, Mar. 2019.
[25] Q. Wang, C. Yang, H. Wang, Z. Cui, and Z. Gao, "Online monitoring of gas–solid two-phase flow using projected CG method in ECT image reconstruction," *Particuology*, vol. 11, no. 2, pp. 204–215, Apr. 2013.
[26] J. Zhao, Y. Xu, C. Tan, and F. Dong, "A fast sparse reconstruction algorithm for electrical tomography," *Meas. Sci. Technol.*, vol. 25, no. 8, 2014, Art. no. 085401.
[27] M. A. T. Figueiredo, R. D. Nowak, and S. J. Wright, "Gradient projection for sparse reconstruction: Application to compressed sensing and other inverse problems," *IEEE J. Sel. Topics Signal Process.*, vol. 1, no. 4, pp. 586–597, Dec. 2007.
[28] P. C. Hansen, *Discrete Inverse Problems: Insight and Algorithms*. Philadelphia, PA, USA: SIAM, 2010.
[29] J. M. Bioucas-Dias and M. A. T. Figueiredo, "A new TwIST: Two-step iterative shrinkage/thresholding algorithms for image restoration," *IEEE Trans. Image Process.*, vol. 16, no. 12, pp. 2992–3004, Dec. 2007.
[30] Z. Cui, H. Wang, Z. Chen, Y. Xu, and W. Q. Yang, "A high-performance digital system for electrical capacitance tomography," *Meas. Sci. Technol.*, vol. 22, no. 5, 2011, Art. no. 055503.

SHOUXIAO LI received the M.Sc. and Ph.D. degrees from Tianjin University, China, in 2009 and 2012, respectively. He is currently a Lecturer with the College of Computer and Information Engineering, Tianjin Agricultural University. His current research interests include process tomography, artificial intelligence, and multiphase flow measurement.

HUAXIANG WANG (Senior Member, IEEE) is currently a Professor with the School of Electrical and Information Engineering, Tianjin University. His research interests include sensing techniques and information processing, process parameter detection and control systems, and intelligent instrumentations.

TONGHAI LIU received the Ph.D. degree from China Agricultural University, China, in 2013. He is currently a Professor with the College of Computer and Information Engineering, Tianjin Agricultural University. His current research interests include intelligent detection, artificial intelligence, and agricultural big data.

ZIQIANG CUI (Member, IEEE) received the M.Sc. and Ph.D. degrees from Tianjin University, China, in 2007 and 2009, respectively. He is currently an Associate Professor with the School of Electrical and Information Engineering, Tianjin University. His current research interests include electrical tomography instrumentation, signal processing, sensor design, and multi-phase flow measurement.

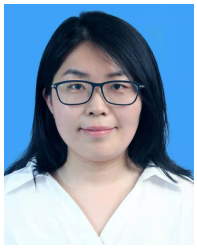

JOANNA N. CHEN received the Ph.D. degree from Nankai University, China, in 2015. She is currently a Lecturer with the College of Science, Tianjin University of Technology. Her current research interest includes bijective combinatorics.

ZIHAN XIA received the B.Sc. degree from North China Electric Power University, China, in 2017. He is currently pursuing the master's degree with the School of Electrical and Information Engineering, Tianjin University. His current research interests include process tomography, artificial intelligence, and multi-phase flow measurement.